Allosteric Activation of p300 Autoacetylation by the Tumor Suppressor p53

Stephanie Kaypee[1], Raka Ghosh[2], Smitha Asoka Sahadevan[1], Manidip Shasmal[2], Piya Ghosh[2], Neeladri Roy[2], Jayati Sengupta[3*], Siddhartha Roy[2*], and Tapas K. Kundu[1*]

[1]Transcription and Disease Laboratory, Molecular Biology and Genetics Unit, Jawaharlal Nehru Centre for Advanced Scientific Research, Bangalore, Karnataka, India;
[2]Department of Biophysics, Bose Institute, Kolkata, India;
[3]Division of Structural Biology and Bioinformatics, CSIR-Indian Institute of Chemical Biology, Kolkata, India.

***Corresponding Authors**

Correspondence: Tapas K. Kundu: tapas@jncasr.ac.in, Siddhartha Roy: sidroykolkata@gmail.com, and Jayati Sengupta: jayati@iicb.res.in

Keywords: Epigenetics; Histone acetylation; Tumor suppressor; Transcription; Enhancer; Gene regulation

Abstract

The transcriptional coactivator p300 (KAT3B) is an essential protein with an intrinsic lysine acetyltransferase activity. As a coactivator, p300 is essential for p53 transactivation; however, its precise role in p53 transactivation remains unclear. Here, we report that in addition to being a substrate, p53 allosterically activates the acetyltransferase activity of p300. Mechanistically, the activation occurs through the enhancement of p300 autoacetylation. Cryo-electron microscopic analysis of the p53-p300 complex revealed that the domain organization of p300 is substantially altered upon binding of p53, suggesting a p53-induced 'conformational switch' in the p300 structure, between an inactive and a catalytically active form. Analysis of the genome-wide occupancy of autoacetylated p300 after p53-mediated activation revealed enrichment of acetylated p300 near the transcription start sites of many p53-regulated genes. This is accompanied by a similar enrichment of activating histone marks near those sites. We conclude that allosteric activation of p300 by p53 allows p300 to be hyperactive only near the region of p53 regulated genes, thus, imparting an additional layer of specificity enhancement mechanism in the regulation of gene expression. Such a mechanism could be an important component of imparting locale-specific alteration of other epigenetic marks.

Introduction

Organismic complexity scales with the intricacies and sophistication of gene regulation. How this intricate regulation is achieved, however, is not fully understood. Specificity, both spatial and temporal, is at the heart of this extraordinarily elaborate and complex regulatory process (1). Protein-protein interactions among multiple transcription factors bound to adjacent sequences, DNA-mediated cooperativity and other factors have been found to enhance site selectivity, and to initiate the assembly of multi-protein regulatory complexes. After assembly the regulatory complex initiates the recruitment of co-activators, chromatin modifiers and other factors, thereby increasing chromatin accessibility and the initiation of RNA synthesis (2, 3). It is not known whether any steps beyond the assembly of regulatory complexes influence the spatial and temporal specificity of gene regulation.

p300 (KAT3B) is a transcriptional co-activator with intrinsic acetyltransferase activity. Being a large adaptor protein, p300 bridges the basal transcription machinery to DNA sequence-specific transcription factors (4-6). By virtue of its structural plasticity, p300 can interact with the intrinsically disordered transactivation domains of a vast array of transcription factors, thereby functioning as a nodal integrator of signals terminating in regulation of transcription (7-11). Therefore, its recruitment via the interaction with sequence-specific transcription factors can regulate transcription from the chromatin template (12).This protein is often recruited to assembled regulatory complexes, where it acetylates histone tails in the vicinity. In this way, p300 promotes localized chromatin accessibility and, subsequently, selective transcriptional initiation (13).

The basal catalytic activity of p300 is enhanced by *trans*-autoacetylation of its lysine-rich regulatory loop (14). It had been proposed that in the absence of acetylation, the positively charged lysine-rich auto-inhibitory loop folds back onto the enzyme active site, thus hindering optimal substrate-enzyme interaction. Since p300 is involved in diverse physiological roles, the precise regulation of its function is essential. It has been demonstrated that some factors affect the levels of p300 autoacetylation in the cell. Intriguingly, these factors have distinct cellular functions and induce p300 autoacetylation under different cellular contexts. The Anaphase Promoting Complex/Cyclosomes (APC/C) subunits APC5 and APC7 are capable of enhancing p300 autoacetylation which is required for proper cell cycle progression (15). Similarly, the transcription factor, MAML1, has been shown to increase the levels of p300 autoacetylation thereby inducing the transcription of Notch pathway genes (16). During cellular stress, GAPDH associates with the E3 ligase,

Siah1, and shuttles to the nucleus, where it enhances p300 autoacetylation which in turn activates the p53-mediated apoptotic pathway (17). p300 autoacetylation is negatively regulated by the Class III lysine deacetylase, SIRT2 and as expected, the suppression of p300 autoacetylation leads to the reduction of its enzymatic activity (18). We have previously reported the presence of global histone hyperacetylation in oral cancer. Mechanistically, this abnormality is a consequence of enhanced p300 autoacetylation, which is induced by NPM1 and nuclear GAPDH in a nitric oxide (NO) signaling-dependent manner. Autoacetylated p300 may be the driving force that causes alterations in the epigenetic landscape and, consequently, the global deregulation of transcription that is required for oral carcinogenesis (19). Thus, regulation of p300 autoacetylation may be a key factor in regulation cellular responses.

In the present study, we addressed the mechanism of factor-induced p300 autoacetylation and its importance in p53-dependent gene regulation. We found that the master tumor suppressor protein p53 specifically induces p300 autoacetylation. To gain the mechanistic insights of the induction of autoacetylation, we have solved the structure of p300-p53 complex by cryo-electron microscopy. These data revealed that p300 undergoes substantial conformational rearrangements of its domains, thus leading it to adopt an active 'open' conformation. Comparison of genomic distribution of autoacetylated p300 and p300 before and after stimulation by p53 indicates that autoacetylated p300 is specifically and uniquely present around transcription start sites (TSS) of p53 regulated genes. This study establishes the first account of p53-mediated induction of p300 autoacetylation and its chromatin recruitment at transcriptional regulatory elements. The implications of these observations for the specificity of gene regulation are further explored.

Results

p53 directly modulates p300 autoacetylation and acetyltransferase activity

To explore whether p53 has an effect of acetyltransferase activity of p300, an *in vitro* acetyltransferase assay was designed to detect the effect of p53 on the levels of p300 autoacetylation. p53 specifically induced the autoacetylation of 20 nM p300 in a concentration-dependent manner (ranging from 40 nM to 160 nM p53 monomers) but exhibited a negligible effect on the autoacetylation of the other two classes of KATs, PCAF and Tip60 (Fig. 1A). An approximately 4.5-fold enhancement of p300 autoacetylation was observed in the presence of 160 nM p53 (4:1 ratio of p53 tetramers to p300). Because p53

forms a stable tetramer and may possibly interact with p300 as a tetramer (20), a significant degree of p300 autoacetylation was reached only when p53 was present in a 1:1 ratio of tetrameric p53 to p300. At a suboptimal concentration (40 nM) of p53, (tetrameric p53 to p300 ratio of 0.5:1), a negligible increase in the autoacetylation was observed (Fig. 1B). Moreover p53 is a substrate of most major nuclear KATs, including p300/CBP (21), PCAF (KAT2B) (22), TIP60 (KAT5) (23, 24), MOZ (KAT6A) (25) and MOF (KAT8) (23). Therefore, the specificity exhibited by p53 toward the enhancement of p300 autoacetylation, with no effect seen for PCAF and Tip60, led us to conclude that p53 is not merely a substrate of p300 but a regulator of the intrinsic enzymatic activity of p300. This specific role of p53 was investigated further. Three different substrates of p300, p47 (N-terminal truncated (Δ40p53) isoform of p53, incapable of binding to p300), Positive Coactivator 4 (PC4) and p50 (a subunit of NFκB) were also tested and found not to effectively induce p300 autoacetylation (Fig. S1A-C). To investigate the effect of the p53-mediated induction of p300 autoacetylation, we performed an *in vitro* histone acetyltransferase assay using recombinant histones as the substrate. In agreement with the results of the autoacetylation assay, we observed an approximate 3-fold increase in p300 histone acetyltransferase at a p300: p53 in a molar ratio of 1:2. Notably, we observed an approximate 4.5-fold increase in p300 activity in the presence of p53, thus suggesting that p53 positively modulates p300 KAT activity through the induction of autoacetylation. Further increases in the p53 concentration did not affect the HAT activity beyond 4.5-fold (Fig. 1C). The *in vitro* p53-mediated induction of p300 autoacetylation was further verified in the cellular context. Endogenous p53 levels were stabilized in HepG2 cells by using the small molecule inhibitor of the MDM2-p53 interaction, Nutlin-3a. The stabilization of p53 after Nutlin-3a treatment appeared to positively regulate the levels of p300 autoacetylation in the cells in comparison to DMSO-treated or untreated cells (Fig. 1D). Furthermore, the fluorescence intensity due to p300 autoacetylation was significantly ($p<0.001$) enhanced in HepG2 cells treated with Nutlin-3a expressing wild-type p53 (Fig. S1D, E). We observed mild toxicity after treatment with 10 μM Nutlin-3a, a result that may account for the marginal decrease in p300 autoacetylation observed in this treatment condition compared with 5 μM Nutlin-3a (Fig. S1D, E). We expected that hyper-autoacetylated p300 would induce p300-specific histone acetylation in cells. To address this possibility, histone acetylation at H3K9 and H3K14 were investigated in the presence and absence of Nutlin-3a (Fig. 1E). It has been previously demonstrated that p53 acetylation and histone acetylation increase after Nutlin-3a treatment (26). Therefore, to test for whether the enhancement in histone acetylation was due to the p53-mediated

enhancement of p300 autoacetylation, we treated p53-null H1299 cells with Nutlin-3a and probed for the levels of different histone acetylation marks in treated versus control cells (Fig. 1F). Interestingly, we found that the histone acetylation levels did not show any appreciable alteration in Nutlin-3a-treated H1299 cells, thereby signifying the importance of p53 in the activation of p300 KAT activity. To rule out the possibility that p300 might be transcriptionally regulated by p53 rather than post-translationally modulated, p300 transcript levels were compared between cells treated with Nutlin-3a and DMSO. No change in p300 transcript levels was observed in the presence of p53 compared to p21 (an early p53 target gene) transcripts, thus suggesting that p300 is not regulated by p53 at the transcriptional level (Fig. S1F). The observation was confirmed in H1299 doxycycline-inducible p53-expression cells, in which the levels of p21 were significantly upregulated after doxycycline treatment while p300 transcript levels remained unchanged (Fig. S1G). Collectively, these results established p53 as a *bona fide* inducer of p300 autoacetylation and its acetyltransferase activity.

To elucidate the mechanistic details of p53-mediated activation of p300, the importance of the direct interaction between p53 and p300 was investigated. p53 directly contacts p300 through four important residues (L22, W23, W53, F54) in its transactivation domain. Mutations in these residues severely compromise p53 transactivation (20). After DNA damage, p53 is phosphorylated by several kinases, and phosphorylated p53 binds to its coactivator p300 with higher affinity (27, 28). Interestingly, the higher the number of phosphorylated sites on the p53 N-terminus, the higher its affinity for CBP/p300 (28, 29). A triple-phospho-mimic peptide (S15E, T18E, S20E) comprising of the 11th to 30th amino acid residue of the p53 (TAD1 domain) protein along with a cell penetrating sequence and NLS was used to obstruct the interaction between p53 and p300 (30) (Fig. S2A, Table S1). Using a filter-binding assay-based strategy, the importance of the p53-p300 interaction for the activation of p300 was assessed on the basis of the level of p300-mediated histone acetylation (Fig. 1G). The peptides and p53 alone did not bind to the p81 phosphocellulose filters; therefore, the measured radioactivity was only from the tritium-labeled acetylated histones bound to the filters. The basal activity of p300 in the absence of any inducer was considered as 100% activity, and the peptides alone did not alter the activity of p300, thus signifying that any change in histone acetylation observed thereafter was a direct consequence of the p300-p53 interaction. In the presence of 4 nM p53, a 3-fold increase in the histone acetylation was observed. The presence of scrambled peptide did not alter the p53-mediated induction of

p300 activity, but triple phospho-mimic p53 peptides (3E pep) effectively decreased histone acetylation levels. These results indicated that the 3E phospho-mimic p53 peptide effectively interfered with the p53-p300 interaction, thus presumably leading to decreased p300 autoacetylation and activity, as indicated by a significant decrease in histone acetylation levels. The scrambled peptide exhibited a negligible effect on p53-mediated p300 activation, thus ensuring that the decrease observed in the case of the phospho-mimic peptide was indeed due to the disruption of the p53-p300 axis and was not a non-specific effect of the peptides (Fig. 1G). Furthermore, to ascertain whether these peptides were effective in cells, HepG2 cells were treated with Nutlin-3a to stabilize the levels of p53. The cells were then treated with different concentrations of the 3E phospho-mimic p53 peptide, which has cell-penetrating sequences (Fig. 1H). The levels of p53 increased after Nutlin-3a treatment, and the peptide treatment did not alter p53 protein levels. Therefore, the mimic p53 peptides did not alter cellular p53 protein levels, and the observed alteration in histone acetylation is a direct consequence of the disruption of p53-p300 interaction. In agreement with the previous observation, the H2AK5 acetylation increased on p53 stabilization with Nutlin-3a (Fig. 1H, S2B). After treatment with the interfering peptide, the levels of H2AK5 acetylation gradually decreased in a concentration-dependent manner (Fig. 1H), whereas H2AK5ac levels remained unchanged after scrambled peptide treatment (Fig. S2B). To address whether tetrameric p53 was indeed important for the induction of p300 autoacetylation, we used a p53 mutant that could not form stable tetramers. Because tetrameric p53 is the form that interacts with p300 (31), we used a tetramerization-defective mutant, L344A, to address the importance of p53 oligomerization on the induction of p300 autoacetylation. When H1299 cells were transfected with this mutant, we observed no enhancement in the global levels of p300 autoacetylation or any alteration in p300 protein levels (Fig. S2C-F). These experiments revealed the importance of p53 tetramerization and the requirement for the direct interaction between p53 and p300 for p300 autoacetylation and augmentation of its acetyltransferase activity.

Cryo-EM reveals conformational changes in p300 domains after p53 binding

Based on the results of the previous experiments it was evident that the interaction of p300 with p53 enhances its autoacetylation as well as its acetyltransferase activity toward other substrates. A plausible hypothesis is that p53 binding stimulates p300 activity through a structural switch, resulting in an active p300 conformation. To obtain structural evidence regarding any possible conformational change in p300 after interaction with the p53 tetramer,

we have generated cryo-EM maps of p300 alone (Fig. 2A,B) and in complex with p53 (Fig. 2C,D) (resolutions of 9.8 Å and 10.7 Å at FSC = 0.143 cut off, and 13.5 and 15.7 Å at FSC = 0.5 cut off for p300 and the p53-p300 complex respectively; Supplemental Fig. S3R, Q). To ensure the reliability of the maps, we used several validation strategies (see Experimental Procedures and Fig. S3A-P).

On the basis of the size of the enclosed volume, the molecular mass of the p300 density map (~233 kDa estimated from the occupied volume, with 0.82 D/Å^3 as the protein density) was somewhat smaller than the known molecular mass of p300 (264 kDa). Evidently, the long unstructured regions at the N- and C-termini (~650 amino acids, equivalent to ~70 kDa; Fig. S3T) were not entirely visible in our reconstruction, possibly because of their dynamic nature. Considering that the p300 map encompassed only the structured domains, the effective molecular mass was adequate. A cryo-EM study of the estrogen-coactivator complex has recently reported that the full-length p300 forms a rather compact yet flexible conformation when present outside the complex, thus indicating the intrinsically disordered nature of the protein. Some of the features of the present reconstruction matched with the p300 cryo-EM map (32). However, the size of the previous map was much larger, thereby suggesting that the density of the previous map presumably encapsulates almost the entire protein.

The p300 density map showed a 'fist-like' appearance with a 'thumb' feature (Fig. 2A, B), whereas the p53-p300 complex adopted a shape similar to that of a kettle, with a protruded 'spout' in the middle and a 'handle' at the side (Fig. 2C, D). Compared with the p300 in complex with p53, the free protein appeared more compact when the two maps were juxtaposed (Fig. 2E). Comparison of the two maps clearly showed significant structural rearrangements in p300 following p53 binding. A bi-lobed density corresponding to the p53 tetramer was visible in the cryo-EM map of the complex, and the p300 and p53 segments were computationally separated (Fig. 2F) by using a cluster segmentation procedure implemented in SPIDER (33). The overall topology of the p53-p300 complex (Fig. 2F) appeared to be very similar to that of the predicted model in a previous structural study (20). The centrally located, protruding density (termed here as 'spout') was the structural hallmark in the density map of p300 in complex with p53 (Fig. 2C, F and S3S).

Activation of p300 by allosteric binding of p53

A prediction regarding the elusive 'active' p300 conformation has been made in a previous analysis of the p300 core domain crystal structure by Delvecchio *et al*, in which the authors

have suggested that free p300 may be present in an inactive conformation (34). However, the molecular events underlying factor-induced p300 autoacetylation are not clearly understood. To dissect the mechanistic details of the p53-induced activation of p300 autoacetylation, we attempted to interpret the cryo-EM densities in molecular terms. Available atomic structures of different domains were used to identify the location of this domain within the EM density envelopes. The bromo-HAT-RING-PHD domains of p300 comprise the central domain, while the KIX and TAZ1 domains are at the N-terminal, and the TAZ2 and IBiD domains belong to the C-terminal part (Fig. S3T). A crystal structure of the central domain in 'auto-inhibited' conformation is available (pdb: 4BHW), where PHD and RING domains are loosely packed on the HAT domain. The structure shows a 'kink' between the bromo and HAT domains (Fig. S3V).

The crystal structure of the central domain when fitted in Chimera (35) as a rigid body into the free p300 density map (CC = 0.88), it could satisfactorily be fitted in the central region of the density (Fig. 3A and Fig. S3W). The HAT occupied the 'palm' while bromo-domain was placed in the 'fingers' of the 'fist' (Fig. S3V-W) keeping the 'kink' between HAT and bromo-domain the same as seen in the crystal structure.

The protruded feature ('spout') in the density map of p300 in complex with p53 (Fig. 2C and S3S) showed striking resemblance with the shape of the bromo-domain (Fig. S2S, V). However, to accommodate the bromo-domain into that density, opening of the 'kink' between HAT and bromo-domain was obligatory (Fig. 3B, Fig. S3S). Thus, the p300 in the p53-p300 complex manifested its 'open' conformation revealing the protruded shape ('spout') of the bromo-domain prominently (Fig. 3D). Furthermore, the densities corresponding to the RING and PHD domains were seen at the junction of 'fist' and 'thumb' in the p300 map, whereas no such densities were visible in the same region of the complex (Fig. 3A). Instead, weak densities were observed at the top of the bromo-domain (Fig.3B). Apparently, the PHD and RING domains were displaced (Fig. 3C) in a similar manner to that proposed in a recent study (34).

On the basis of the cylindrical shape of KIX (the N-terminal domain preceding the bromo domain), the 'thumb' density was assigned to KIX (Fig. S4A). A triangular shaped density resembling the structure of the TAZ domain apparently fastened the HAT domain in a 'closed conformation' of the protein which opened up in the complex (Fig. S4B). Overall, it appeared that the 'autoinhibited' inactive conformation described in the crystal structure was further stabilized by other domains of the protein. A clear loop-like density was seen at the back of the HAT domain in the complex (Fig. 2D, 3E). The lysine-rich autoinhibitory loop could be

placed inside this density after a rotation along the HAT domain axis. We speculate that, while transforming into the 'open' conformation upon interactions with p53, the HAT domain of p300 rotates and exposes the autoinhibitory loop (Fig. 3E).

Distinct features of the p53 tetramer were identifiable in the cryo-EM map of the p53-p300 complex. In the previously analyzed p53 tetramer structures (without DNA or DNA-bound maps, approximately 6-8 nm, (36)) the four DNA-binding domains remain closely packed, while the tetramerization domains are displaced out of the plane (Fig. S5). However, in the present map of p53-p300 complex (approximately 12 nm), the p53 adopted a distorted shape (Fig. S4C), with two side-lobes exhibiting a centrally connected density attributable to the packed tetramerization domains (pdb: 4D1M; Fig. S4E). Each side lobe of p53 density in our cryo-EM map was composed of a dimer of DNA-binding domains (presumably along with the N-terminal domains; Fig. S4C). A segment of DNA could be accommodated in the cleft created by the two side lobes (Fig S4D).

A previous model has proposed that the p300 monomer wraps around the p53 tetramer. In this model, the N-terminal KIX and TAZ1 domains and the C-terminal TAZ2 and IBiD domains of p300 interact with p53, with the TAZ2 interaction being the strongest, followed by the interactions with TAZ1, KIX, and IBiD (20). Our map of the p53-p300 complex (CC with the density envelope = 0.9) not only provided experimental evidence of this proposed model but also elucidated the dynamic mechanism of factor-induced p300 autoacetylation.

Redistribution of p300 after autoacetylation and p53-mediated activation

If the p53-mediated allosteric activation of p300 is important for p53 mediated regulation of targeted genes, then it is expected that activated forms should be present in the vicinity of the regulated genes. We have thus attempted to explore the effect of p53 expression on presence p300 in different genomic sites. The differential occupancy of acp300 and p300 on the promoters of genes that are expressed after p53 stimulation has been investigated. The enrichment patterns indicated a distinct preference of acp300 for the promoter proximal regions, after p53 expression, whereas only a weak enrichment pattern was observed for p300, thus reinforcing the possibility that the autoacetylated form of p300 is actively associated with p53-mediated transcriptional initiation (Fig. 4A). We analyzed the differential occupancy of p300 and acp300 with publically available datasets of RNAPII, H3K27ac and H3K4me1 distribution. The abundance of acp300 at the promoters correlated with the presence of RNA Pol II enrichment and active promoter marks such as H3K27ac (Fig. 4A). These data indicated a specific role for acp300 within the entire pool cellular p300. The

coactivator occupancy has been integrated with the microarray expression analysis of the p53-induced differentially expressed genes (37), revealing a greater overlap between the p53-driven transcription and acp300 (4341 genes) recruitment (Fig. S6A-C) in comparison to p300 (1950 genes) (Fig. 4B).

We hypothesize that after p53 is stabilized in the cell or overexpressed, it associates with its ubiquitously expressed co-activator p300. This association triggers an allosteric conformational switch in p300, thereby enhancing intermolecular autoacetylation. It is this catalytically active form of p300 that is subsequently enriched in p53-target gene regulatory chromatin regions via its interaction with p53. The active, autoacetylated p300 then acetylates histone tails at these loci, decompacting chromatin and leading to enhanced transcription p53-dependent and (possibly) independent gene-networks (Fig. 4C, Table S2).

Discussion

The functional crosstalk between p300 and p53 is well established; however, the role of p53 in the modulation of the enzymatic activity of p300 has not been addressed before. The ChIP-seq analysis of acp300 genome occupancy after p53 induction provided further insights into the transcriptional cascades triggered by effector (p53)-mediated induction of p300 autoacetylation. p300 autoacetylation can control its catalytic activity (14), but the dynamics of p300 autoacetylation under physiological stimuli are not fully understood. The present findings provide experimental evidence that establishes p53 as a *bona fide* modulator of p300 autoacetylation. Remarkably, among all of the substrates of p300 tested, only p53 enhanced p300 autoacetylation, thus confirming the molecular specificity of this phenomenon. The preferential induction of p300 autoacetylation by p53 over that of other acetyltransferases further exhibited the specificity of p53-mediated induction of p300 autoacetylation. This result further suggested that the induction of autoacetylation is not merely a by-product of enzyme-substrate interaction. No structural information currently available regarding the full-length p300 and tetrameric p53 complex. By using cryo-EM microscopy, we resolved the structure of p300 and p53 tetramer to gain insights into the molecular mechanisms of p53-induced allosteric activation of p300. Earlier structural studies have shown that the p300 core catalytic domain exists in a compact spatial conformation with basal catalytic activity. In the 'un-activated' conformation, the RING domain forms an obstruction to substrate-binding by occluding the substrate-binding groove of the HAT domain, which is buried inside the compact structure; importantly, this model was corroborated by our cryo-EM structure (34). In the p53-p300 complex, however, a distinct alteration of p300 conformation was observed.

In this structure, the inhibitory RING domain was displaced away from the substrate-binding pocket of the p300 HAT domain in a conformation that could be characterized as ‘open’ and ‘activated’. These cryo-EM structural studies suggest that the ‘open’ conformation of p300 precedes the induction of autoacetylation, which is required for the maximal activation of p300 lysine acetyltranferase activity. The structure of the complex presented here indicated that N-terminal domains of p53 interact first with p300 to induce conformational changes and thereby the C-terminal domains of p53 gain access of the HAT domain of p300 (Fig. S4) suggesting the activation mechanism is allosteric in nature. Therefore, these data indicated that the ability of an effector to modulate the p300 conformational state can directly affects p300 acetyltransferase activity. p300 is recruited to gene promoters by several transcription factors (12, 38) where it can assemble transcription complexes that facilitate gene expression. The autoacetylation of p300 has been proposed to induce distinct structural changes that are critical for its activity. Black *et al.* have shown that the presence of p300 at the PIC exerts an inhibitory effect of transcription *in vitro*. The release of p300 from the complex is attributed to the possible conformational switch in the p300 structure after autoacetylation. It is clear from this study that p300 autoacetylation is essential for maximal transcription to proceed. The predominant occupancy of acp300 on the TSS of the promoters is a novel finding based on the obtained ChIP-seq analysis. These data are in agreement with the factor-dependent recruitment of the acetyltransferases p300/CBP and subsequent gene activation, as previously reported. As shown from our biochemical and structural data, the direct interaction of p53 with its coactivator p300/CBP is functionally important in this process and serves as the mechanism of induction of autoacetylation. Ceschin *et al.* have shown that CBP is methylated at multiple sites by the arginine methyltransferase protein CARM1 and the arginine methylation of CBP stimulates CBP activity through the induction of CBP autoacetylation. Use of polyclonal antibodies recognizing specific CBP methylation species, has indicated that each methylated class of CBP has differential HAT activities and distinct transcriptional effects, thereby diversifying the estrogen receptor response (39). The contextual recruitment of p300 has been noted in another study performed in the MCF7 cell line, in which it has been observed that in resting cells, p300 appears to show a preference towards neural lineage gene promoters, whereas the enrichment of p300 shifts toward estrogen-regulated gene targets after estradiol treatment (40). In a recent report, CBP has been shown to interact with RNAs. At active enhancers, CBP interacts with enhancer RNAs, which bind to the CBP catalytic domain, inducing CBP autoacetylation (41). The resultant enhancement in CBP activity leads to increased histone acetylation and expression of target genes. In the present

work, the differential occupancy of p300 and acp300 was investigated after p53 activation. After autoacetylation, in the presence of p53, p300 appeared to show a strong preference for the TSS (Fig. 4A), in agreement with the recruitment model discussed earlier. The binding of acp300 was strongly associated with RNA Pol II occupancy and the promoter acetylation mark H3K27ac. This finding suggested that acp300 is indeed involved in the assembly of the basal transcription machinery at promoter-proximal regions of genes. The overall pool of p300 did not show an appreciable alteration in chromatin occupancy in the presence of p53, whereas a distinct redistribution in acp300 enrichment was observed. Notably, the integration of the ChIP-seq data with the gene expression microarray analysis revealed that the enrichment of acp300 was a better determinant of p53-mediated gene expression than the presence of unmodified p300. This result was in agreement with previous studies in which p300 has been shown to occupy transcriptionally silent regions or the chromatin, whereas the co-occupancy of (presumably autoacetylated) p300 with its histone acetylation mark H3K27ac was observed at transcriptionally active genes (42). With the current evidence, it can be speculated that the ability to induce structural alterations in p300, leading to enhancement of its acetyltransferase activity, may be a key deciding factor in p300 chromatin recruitment and downstream transcriptional programs. The ChIP-seq data suggest that the phenomenon of factor-induced p300 autoacetylation may play a pivotal role in the integration of stimulus-driven transcriptional pathways. Specifically, the recruitment of the catalytically active form of p300 may trigger a rapid transcriptional response to internal and external signaling cues. In this study, it is the p53-driven pathway that stimulates a burst in autoacetylated p300 levels and an alteration of the epigenetic landscape, which may be essential for these p53 signaling pathways.

The activation of p300 by p53 suggests that p300 may be preferentially activated when it is recruited to p53 at its target sites. This allosteric activation would suggest an enhanced activity of p300 when it is complexed with target-site bound p53, thereby leading to localized transcriptional initiation. Thus, the augmented activity of p300 at genes to which it is recruited by p53 adds another element of specificity beyond that of the transcription factor binding. Moreover, p53 was able to modulate the levels of histone acetylation concomitant with the induction of p300 autoacetylation, thus signifying that the tumor suppressor p53 can alter the epigenetic landscape through the regulation of p300 acetyltransferase activity. We speculate that the allosteric activation of p300 by p53 demonstrated here may be a representative example of a general mechanism for attaining the high degree of spatio-temporal specificity required for attaining exquisite and intricate gene regulation.

Materials and Methods

Antibodies

Anti-p300 Antibody (N-15) was purchased from Santa Cruz (Cat# sc-584). Anti-p53 Antibody, clone DO-1 was purchased from Merck Millipore (Cat# OP43). Secondary antibodies: Rabbit polyclonal antibodies against Histone H3, H3K9ac, H3K14ac, H2AK5ac and K1499ac p300 (anti-acp300) were raised in-house. Goat Anti-Mouse IgG H&L (HRP) (Cat# ab97023) and Goat Anti-Rabbit IgG H&L (HRP) (Cat# ab97051) were purchased from Abcam. Fluorescent-labelled secondary antibodies Goat anti-Rabbit IgG (H+L) Cross-Adsorbed, Alexa Fluor® 488 (Cat# A-11008) and Goat anti-Mouse IgG (H+L) Cross-Adsorbed, Alexa Fluor® 633 (Cat# A-21052) were purchased from Thermo Fisher Scientific.

Cell Culture

Human non-small cell lung carcinoma H1299 cells (ATCC® CRL-5803™) were cultured in RPMI-1640 media supplemented with 2 mM glutamine, 1% antibiotic solution (penicillin, streptomycin, amphotericin) and 10% fetal bovine serum (FBS). The pEBTetD p53 H1299 cells were cultured in supplemented RPMI-1640 under 1.2 μg/ml Puromycin antibiotic selection. Human hepatocellular carcinoma HepG2 cells (ATCC® HB-8065™) were cultured in MEM supplemented with 2 mM glutamine, 1% antibiotic solution (penicillin, streptomycin, amphotericin) and 10% fetal bovine serum (FBS). The cells were grown at 37 °C in 5% CO_2. Full length p300, PCAF and Tip60 were expressed in Sf21 (*Spodoptera frugiperda*) insect cells (ThermoFisher). The cells were grown in Graces' Media containing antibiotic solution (penicillin, streptomycin, amphotericin) and 10% fetal bovine serum (FBS).

Bacterial Cultures

The wt p53 and p53 mutants (T18E p53 and L344A p53) were expressed and purified from BL21 (DE3) pLysS or BL21(DE3) *E. coli* strains.

Cloning of p53 constructs

Wildtype p53 was cloned into BamHI-HF/HindIII-HF sites in pFLAG-CMV™-2 Mammalian Expression Vector (Sigma Aldrich). Phusion DNA polymerase (ThermoScientific) was used for the PCR. Point mutants were generated using Site Directed Mutagenesis (SDM) method. Pfu-Ultra polymerase (Stratagene) was used for the SDM PCR

reaction. Following the PCR, the reaction was treated with DpnI restriction enzyme, for 2 hours at 37 °C. A portion of the reaction mixture was transformed into XL1-BLUE super-competent cells. The point mutants were confirmed by sequencing. The FLAG-tagged p53 construct was subcloned into the Tet-ON mammalian expression plasmid pEBTetD (a kind gift from Prof. Gründemann, University of Cologne, Germany (43)). The construct was amplified using a forward primer designed against the FLAG-tag containing a KpnI restriction site and a reverse primer specific to the 3' end of p53 containing a XhoI restriction site. The primers have been listed in Table S3.

Protein expression and Purification

His_6-tagged full length p300, Tip60 and FLAG-tagged PCAF were expressed by transfection of the respective recombinant baculovirus into Sf21 insect ovary cells. 60 hours post infection the cells were harvested. For the His_6-tagged protein purification, the cells were resuspended in chilled homogenization buffer (20 mM Tris-HCl pH 7.4, 10% glycerol, 2 mM β-mercaptoethanol, 0.2 mM EDTA, 2 mM PMSF, 0.1% NP-40, 50 µg/ml leupeptin and 50 µg/ml aprotinin, 15 mM imidazole and 500 mM NaCl). The cells were lysed on ice in a Dounce's Homogenizer (Wheaton). The lysate was then allowed to bind to the Ni-NTA resin at 4 °C. The bound resin was washed in buffer containing 20 mM Tris-HCl pH 7.4, 10% glycerol, 2 mM β-mercaptoethanol, 0.2 mM EDTA, 2 mM PMSF, 0.1% NP-40, 15 mM imidazole and 300 mM NaCl. The protein was eluted in buffer (20 mM Tris-HCl pH 7.4, 10% glycerol, 2 mM β-mercaptoethanol, 0.2 mM EDTA, 2 mM PMSF, 0.1% NP-40) containing 100 mM NaCl and 250 mM imidazole. For the purification of FLAG-tagged PCAF protein, of the homogenization buffer was composed of 20 mM Tris-HCl pH 7.4, 20% glycerol, 4 mM $MgCl_2$, 2 mM DTT, 0.4 mM EDTA, 20 mM β-glycerophosphate, 0.4 mM PMSF, 0.1% NP-40, 50 µg/ml leupeptin and 50 µg/ml aprotinin and 500 mM NaCl. The FLAG-tagged protein was then allowed to bind to M2 agarose beads (Sigma Adrich) at 4 °C. The protein-bound resin was washed with buffer (20 mM Tris-HCl pH 7.4, 10% glycerol, 2 mM β-mercaptoethanol, 0.2 mM EDTA, 2 mM PMSF, 0.1% NP-40) containing 300 mM KCl, For the His_6-tagged proteins. The bound protein was then eluted from the resin in buffer (20 mM Tris-HCl pH 7.4, 10% glycerol, 2 mM β-mercaptoethanol, 0.2 mM EDTA, 2 mM PMSF, 0.1% NP-40) containing 100 mM NaCl and 150 ng/µl 3X FLAG peptide.

FLAG-p53 and FLAG-p53 mutants were expressed and purified from BL21(DE3)pLysS *E. coli* strain. The expression plasmids were transformed into E.coli and the transformed cells

proteins of interest were expressed by inoculating primary culture with a single colony which was allowed to grow over-night at 37 °C in Luria Broth medium under ampicillin selection (100 µg/ml) in a shaker incubator (180 rpm). The over-night culture was inoculated into a secondary culture (10% inoculum) which was then allowed to grow at 37 °C in LB medium under ampicillin selection till the OD600 reached 0.4. The bacterial culture was then induced with 0.4 mM IPTG, and grown at 30 °C for 4-6 hours. The cells were harvested by centrifugation at 6000 rpm for 10 mins at 4 °C. The pelleted cells were then lysed in lysis buffer (20 mM Tris-HCl pH 7.4, 20% glycerol, 2 mM β-mercaptoethanol, 0.2 mM EDTA, 2 mM PMSF, 0.1% NP-40) containing 300 mM KCl. The resuspended pellet was sonicated (Sonics-Vibra cell). The cell debris was then pelleted from the lysed cell suspension at 16,000 rpm at 4 °C. The following steps were as described above.

Small Molecule Inhibitor or Peptide treatment

HepG2 cells were treated with the small molecule inhibitor Nutlin-3a (5 µM or 10 µM) for 24 hours. The stabilization of p53 and status of p300 autoacetylation and acetylation of p300-substrates were determined by western blotting analysis and immunofluorescence. For the p53-p300 interfering peptides, HepG2 cells were treated with the indicated concentrations of peptides for 24 hours. The induction of wildtype p53 was achieved by treating the cells with Nutlin-3a for 24 hours after peptide treatment. Western blotting analysis was performed to study the effects of the peptides on p53-mediated modulation of p300 activity.

RT-qPCR

Tet-inducible p53 expression H1299 cells were treated with doxycycline for 24 hours. The cells were harvested in Trizol reagent (Thermofisher) and RNA was isolated according to the manufacturers' instructions. The purified RNA was treated with DNase I (New England Biolabs) at 37 °C for 20 min to remove any contaminating DNA. The RNA was again purified using Phenol-Chloroform-Isoamylalcohol (24:25:1) followed by ethanol precipitation at -80 °C overnight. cDNA was prepared using M-MLV Reverse Transcriptase (Sigma Aldrich) and oligo dT (23) primers (Sigma Aldrich). Real Time PCR was performed using SYBR Green (Sigma Aldrich) and mRNA-specific primers (Table S3).

Co-immunoprecipitation

HepG2 cells were treated with 10 µM p53 phosphomimic peptide (3E pep) or the scrambled control for 24 hours. The cells were then treated with 5 µM Nutlin-3a or the vehicle control

(DMSO) for another 24 hours. The cells were harvested and lysed in RIPA buffer (150 mM NaCl, 50 mM Tris-Cl, 1% NP40, 1% sodium deoxycholate, 1 mM EDTA, and Protease inhibitors). p53 was immunoprecipitated using the DO1 antibody (Merck Millipore, Cat# OP43). Western Blotting analysis was performed to determine whether p53 and p300 interaction is disrupted by the p53 phosphomimic peptide.

Acetyltransferase Assays

For the p300, Tip60 and PCAF autoacetylation assay, the reactions were carried out in HAT assay buffer (50 mM Tris–HCl, pH 7.5, 1 mM PMSF, 0.1 mM EDTA, and 10% v/v glycerol) and 100 mM sodium butyrate at 30 °C for 30 min with or without the protein factors tested as autoacetylation inducers. The assay was performed in the presence of 1 µl 4.7 Ci/mmol [^{3}H]-acetyl-CoA (NEN-PerkinElmer) or 1 µl 1.2 mM acetyl-CoA (non-radiolabeled). After the autoacetyltransferase assay, the radiolabeled proteins were processed by fluorography. For the enzyme activity assay, reactions with 1 nM full-length p300 were carried out in HAT assay buffer (50 mM Tris–HCl, pH 7.5, 1 mM PMSF, 0.1 mM EDTA, and 10% v/v glycerol) and 100 mM sodium butyrate at 30 °C for 30 min. The assays were performed with 2 µM histone H3 or highly purified core histones in the presence of 1 µl 4.7 Ci/mmol [^{3}H]-acetyl-CoA. After the HAT activity assay, the reaction mix was spotted on p81 phosphocellulose paper, which was washed in wash buffer (0.05 M sodium bicarbonate and 5 mM sodium carbonate). The spotted paper was dried and incubated in scintillation fluid (0.005% PPO and 5x10-4% POPOP in Toluene). The scintillation counts were measured in a scintillation counter (Wallac 1409 Liquid Scintillation Counter).

Cryo-Electron Microscopy

Sample for cryo-grid preparation

T18E p53, prepared in a buffer containing 10 mM Tris-Cl, 150 mM NaCl, 5 mM $MgCl_2$, 20 µM $ZnCl_2$, 2 mM PMSF, 1mM DTT, pH 7.5, was mixed with 200 nM p300 at a molar ratio 1:1 and incubated at room temperature for 5 min. For cryo-EM, 4 µl homogeneous p53-p300 complex was applied on glow-discharged Quantifoil® holey carbon TEM grids (R2/2, Quantifoil, Micro Tools GmbH, Jena, Germany) coated with a home-made continuous thin layer of carbon followed by blotting and vitrification with a Vitrobot™ (FEI Inc, Hillsboro, Or, USA) and grids were frozen in liquid ethane. Purified p300, diluted to a final concentration of 200 nM in a buffer containing 10 mM Tris-Cl, 150 mM NaCl, 1 mM DTT, 2

mM PMSF pH 8.0, was used for sample preparation. Grids were prepared and sample imaged similarly as p53-p300 complex.

Cryo-EM data collection and 3D image processing

Data collection was performed on a Tecnai Polara microscope (FEI, USA) equipped with a FEG (Field Emission Gun) operating at 300 kV. Images were collected with 4K X 4K 'Eagle' charge-coupled device (CCD) camera (FEI, USA) at ~79000X magnification, resulting in a pixel size 1.89 Å at the specimen level with defocus values ranging from 1.5 to 4.5μm. All images were acquired using low-dose procedures with an estimated dose of ~20 electrons per $Å^2$. Micrographs screening, particle picking were done separately with EMAN2 software (44) and SPIDER (33). Micrographs are selected on the basis of their visual quality, Thon rings in the power spectra and defocus values. Initially, for the complex, 5400 particle were picked manually according to their sizes using the BOXER program from the EMAN2 package with a pixel size of 1.89Å/pixel. Particle screening was done by visual inspection with utmost care so that only complex particles (~ 10-12 nm) were kept and particles of smaller sizes were rejected. 2D, 3D classification and initial model building were performed using EMAN2. The raw particle images were first subjected to multivariate statistical analysis and classification. The starting model was generated by the common line technique from selected 2D class averages. In SPIDER, defocus of each micrograph was estimated on the basis of its 2D power spectrum and then micrographs were divided into groups of similar defocus. Image processing was done using the reference based alignment method, where the initial volume of p53-p300 complex obtained from EMAN2 was used as the reference. Using projections of this model as a template, total 10,088 particles were selected semi-automatically from all the micrographs. The 3D reconstruction was then done following the standard SPIDER protocols for reference-based reconstruction (33). The overall resolution was 15.7 Å using the 0.5 cutoff criteria and 10.7Å using the 0.143 cutoff criteria. Data for the free protein were processed essentially as for the complex described above. Briefly, micrograph screening, particle selection, and 3D reconstruction were done in EMAN2 to generate an initial model. Coordinates of total 16,152 particles, picked manually in EMAN2, were imported in SPIDER for further reference-based particle alignment, 3D reconstruction, and refinement. The resolution of the final map was 13.5 Å using the 0.5 cutoff criteria and 9.8 Å using the 0.143 cutoff criteria.

Validation of initial models

Initial models were generated in EMAN2 from reference free 2D class averages. Validation of the 3D models was done in multiple ways. Reliability of the obtained initial model in EMAN2 was examined by comparing its different views with the reference-free 2D class averages produced in EMAN2, Xmipp (45) RELION (46) and reference-based SPIDER. Further, the 2D re-projections from the 3D maps were consistent with the 2D class averages. We also acquired two sets of images (grid preparation and data collection in different days) for both p300 and p300-p53 complex and processed independently resulting similar initial maps for both. The crystal structure of the Bromo-HAT shows close resemblance with the core structures of p300 in both the maps. We also manually produced another starting model from the crystal structure of the central domain (4BHW) by low pass filtering. 3D Image processing of the p300 dataset using two different starting models resulted similar 3D maps. Reprocessing of the image data of the complex using RELION (46), an alternative image processing software, resulted reconstruction fairly similar in overall structural features.

Model Building

There is no high resolution structure available for either p300 or p53 full length proteins. In order to describe the density maps of the p300 protein and p300-p53 complex in molecular terms we attempted to dock existing crystal structures of different domains of the protein. The procedure is described in Supplementary Methods section.

Chromatin Immunoprecipitation

The cells were cross-linked in 1% formaldehyde. The crosslinking was quenched in 0.125 M glycine, the cells were lysed in SDS buffer, and the chromatin was sheared using a Bioruptor® Diagenode instrument. Five to ten micrograms of antibody was used in each ChIP. The antibody and BSA-blocked protein G sepharose beads were added to the cleared sheared cross-linked chromatin and incubated at 4 °C overnight. The beads were then washed to remove non-specific binding with buffers containing different salt concentrations. The DNA-protein complexes were eluted from the washed beads using a SDS-sodium bicarbonate elution buffer. The eluates and input were de-crosslinked at 65 °C for 4 hours. Proteinase K and RNase H were added to the de-crosslinked lysates. The DNA was extracted using the phenol:chloroform:isoamyl alcohol method. The DNA was precipitated at -20 °C overnight using sodium acetate and glycogen in 100% ethanol. The DNA pellet was washed in 70%

ethanol and dissolved in nuclease-free water. ChIP-qPCR was performed using SYBR Green (Sigma Aldrich) and loci-specific ChIP primers (Table S3).

ChIP-seq and bioinfomatic analysis

Libraries for ChIP-Seq were prepared with KAPA Hyper Prep Kits. The workflow consists of end repair to generate blunt ends, A-tailing, adaptor ligation and PCR amplification. Different adaptors were used for multiplexing samples in one lane. Sequencing was performed on Illumina Hiseq3000/4000 for a single-end 150 run. High quality (HQ) reads with Q20 were generated using NGS QC Tool Kit v.2.3.3 (47). Filtered reads were aligned against *Homo sapiens* Ensembl build GrCh37 allowing 2 mismatches (-n 2) using the alignment tool Bowtie (48). Post alignment processing including SAM to BAM conversion along with sorting and PCR duplicate removal is performed using SAMTOOLS (49). BAM files of replicates were merged to get merged Input and IP BAM files for acp300 and p300. Peak calling is performed using MACS14 (50) using parameters mfold= 3:10 and p-value of 1e-5 (0.00001). The p300 and acp300 peaks were visualized using the Integrated Genome Viewer (IGV) tool (51). HOMER tool (52) was used for finding overlapping genes within distance of 100 bp overlap within acp300 and p300 and to find unique genes specific to acp300 and p300. Total number of peaks obtained were annotated using Peak Analyser v1.4 (53). Bedgraph files from the peak bed file generated using BEDTOOLS sortBed and GenomeCoverageBed commands. Integration of gene expression data from microarray analysis with ChIP-seq gene enrichment data is carried out to check for the binding occupancy and gene regulation. Average profiles and heatmaps were generated showing ChIP signal densities spanning 5 kb upstream and downstream of TSS using ngs.plot.r (54).

Publicly available datasets/ Deposited data

The ChIP-seq data for p300 and autoacetylated p300 is available at NCBI, SRA Accession ID: SRR5831017. The ChIP-seq data for RNA Pol II, H3K27ac, and H3K4me1 were retrieved from Data Bank of Japan (DDBJ), accession number: DRA001860 (http://dbtss.hgc.jp/) (55). Microarray of inducible p53 H1299 cell line data: GEO: GSE57841 (37). The cryo-EM density maps and coordinates of p300-p53 complex and free p300 were deposited in the Electron Microscopy Data Bank (EMDB) under the accession numbers EMD-6791 and EMD-6792, and deposited in the RCSB Protein Data Bank (PDB) under the accession codes 5XZC and 5XZS, respectively.

Statistics

Unpaired two-tailed t-test has been used for the statistical analysis. The p-values have been indicated in the figures, legends, and methods.

Acknowledgements

This work was supported by Jawaharlal Nehru Centre for Advanced Scientific Research (JNCASR), Department of Biotechnology (DBT) (Programme Support on 'Chromatin and Disease' Grant No. BT/01/CEIB/10/III/01), the Council of Scientific and Industrial Research (CSIR), Government of India (Network Project 'UNSEEN' (BSC0113)) and CSIR-Indian Institute of Chemical Biology. SK is supported by University Grant Commission (UGC) and RG and SM are supported by CSIR, Government of India. TKK and SR are Sir J. C. Bose Fellows. We acknowledge Mr. Madavan Vasudevan and Ms. Madhura Tathode, Bionivid Technology Pvt. Ltd., for the ChIP-seq analysis. We thank Mr. Chiranjit Biswas for cryo-EM data collection and Mr. Sayan Bhakta for troubleshooting during image processing. We acknowledge Dr. Dirk Gründemann (University of Cologne, Germany) for the pEBTetD SLC22A1 construct. We have used illustration templates from the website somersault1824 (http://www.somersault1824.com) available under a Creative Commons Attribution-Noncommercial-Share Alike license (CC BY-NC-SA 4.0) in the model (Fig. 4C).

Figure Legends

Fig. 1: The tumor suppressor p53 enhances p300 autoacetylation. (A) An *in vitro* acetyltransferase assay was performed to determine the levels of autoacetylation of different lysine acetyltransferases (KAT) in the presence of recombinant p53. The autoradiograms indicate the levels of p300, PCAF, and Tip60 autoacetylation respectively; while the Coomassie stained protein panels show the loading control. (B) Graphical representation of the mean fold change± SD of the levels of autoacetylation of each KAT, measured by the relative band intensities, statistical analysis was performed using two-tailed unpaired t-test (*, $p<0.05$, **, $p<0.01$). (C) Enhancement of p300 catalytic activity in the presence of increasing concentrations of p53 as indicated was determined by filter binding histone acetyltransferase assay. The mean fold change was plotted ± SD, statistical analysis was performed using two-tailed unpaired t-test (*, $p<0.05$; **, $p<0.01$; ***,$p<0.001$). (D) Immunoblots showing the levels of autoacetylated p300, p300 and p53 in HepG2 cells treated with DMSO (vehicle control) or Nutlin-3a. Tubulin was used as the loading control. Western blots showing the

levels of histone acetylation levels in (E) HepG2 and (F) H1299 cells treated with DMSO or Nutlin3a as indicated. (G) Results of filter binding assay indicate that the phosphomimic p53 N-terminal peptide can effectively reduce the activity of p300 by interfering with its interaction to p53. The mean fold change was plotted ± SD, statistical analysis was performed using two-tailed unpaired t-test (*, $p<0.05$). (H) HepG2 cells treated with Nutlin-3a and p53 phosphomimic peptide as indicated, and the levels of H2AK5ac, H3, p53, and tubulin were probed by immunoblotting. DMSO treated cells were used as the control.

Fig. 2: Cryo-EM 3D reconstructions of p300 and p300-p53 complex.

(A) Front and B) back view of 3D cryo-EM map of p300 (surface representation in dark cyan). (C) Front and (D) back view of the density map of p300-p53 complex (purple surface). Land marks in p300: F, fist; Th, thumb; and P, palm. In complex: SP, spout; H, handle. (E) Superimposition of the p300 map (dark cyan) on the p300-p53 complex map (purple mesh) reveals that substantial conformational changes occur in p300 upon p53 binding. The asterisk (*) indicates absence of density in the p300 map, whereas in complex, density can be clearly seen in this region. (F) Surface representation of the densities encompassing p300 (blue) and p53 (brick red) in the complex following segmentation.

Fig. 3: Interpretation of the densities in molecular terms.

Stereo representation of (A) p300 map (cyan mesh) and (B) the difference map corresponding to the p300 density obtained from the complex map (blue mesh). Both maps are fitted with crystal structure of various domains of p300 (pdbs: 5HOU, 4BHW, 2LQH, and model of autoinhibitory loop generated by PHYRE2). Bromo, RING, PHD, HAT domains, and autoinhibitory loop are shown in yellow, green, orange, red and violet respectively and other p300 domains are colored grey. Close up views of the superposed cryo-EM maps of p300 and p300-p53 complex (blue mesh: p300 map; purple mesh: p300-p53 complex map) showing rearrangement of (C) RING (green) and PHD domain (orange); Conformational changes in (D) Bromo (yellow) and (E) HAT domain (red) along with autoinhibitory loop (violet) following complex formation with p53.

Fig. 4: Redistribution of p300 after p53-mediated enhancement of p300 autoacetylation.

(A) Heatmaps depicting the enrichment of acp300, p300, H3K27ac, RNA Polymerase II (RNAPII), and H3K4me1 at promoters (TSS±5 kb). (B) Venn diagram showing the overlap between the up-regulated genes enriched at the promoters with both acp300 and p300 and

genes unique to each set. (C) Model depicting the physiological significance of p53-mediated enhancement of p300 autoacetylation.

References

1. Levine M & Tjian R (2003) Transcription regulation and animal diversity. *Nature* 424(6945):147-151.
2. Schneider R & Grosschedl R (2007) Dynamics and interplay of nuclear architecture, genome organization, and gene expression. *Genes Dev* 21(23):3027-3043.
3. Dulac C (2010) Brain function and chromatin plasticity. *Nature* 465(7299):728-735.
4. Bannister AJ & Kouzarides T (1996) The CBP co-activator is a histone acetyltransferase. *Nature* 384(6610):641-643.
5. Chan HM & La Thangue NB (2001) p300/CBP proteins: HATs for transcriptional bridges and scaffolds. *J Cell Sci* 114(Pt 13):2363-2373.
6. Ogryzko VV, Schiltz RL, Russanova V, Howard BH, & Nakatani Y (1996) The transcriptional coactivators p300 and CBP are histone acetyltransferases. *Cell* 87(5):953-959.
7. Bedford DC, Kasper LH, Fukuyama T, & Brindle PK (2010) Target gene context influences the transcriptional requirement for the KAT3 family of CBP and p300 histone acetyltransferases. *Epigenetics* 5(1):9-15.
8. Dyson HJ & Wright PE (2016) Role of Intrinsic Protein Disorder in the Function and Interactions of the Transcriptional Coactivators CREB-binding Protein (CBP) and p300. *J Biol Chem* 291(13):6714-6722.
9. Perissi V, *et al.* (1999) Factor-specific modulation of CREB-binding protein acetyltransferase activity. *Proc Natl Acad Sci U S A* 96(7):3652-3657.
10. Lee CW, Sørensen TS, Shikama N, & La Thangue NB (1998) Functional interplay between p53 and E2F through co-activator p300. *Oncogene* 16(21):2695-2710.
11. Ravi R, *et al.* (1998) p53-mediated repression of nuclear factor-kappaB RelA via the transcriptional integrator p300. *Cancer Res* 58(20):4531-4536.
12. Kundu TK, *et al.* (2000) Activator-dependent transcription from chromatin in vitro involving targeted histone acetylation by p300. *Mol Cell* 6(3):551-561.
13. Vo N & Goodman RH (2001) CREB-binding protein and p300 in transcriptional regulation. *The Journal of biological chemistry* 276(17):13505-13508.
14. Thompson PR, *et al.* (2004) Regulation of the p300 HAT domain via a novel activation loop. *Nature structural & molecular biology* 11(4):308-315.
15. Turnell AS, *et al.* (2005) The APC/C and CBP/p300 cooperate to regulate transcription and cell-cycle progression. *Nature* 438(7068):690-695.
16. Hansson ML, *et al.* (2009) The transcriptional coactivator MAML1 regulates p300 autoacetylation and HAT activity. *Nucleic Acids Res* 37(9):2996-3006.
17. Sen N, *et al.* (2008) Nitric oxide-induced nuclear GAPDH activates p300/CBP and mediates apoptosis. *Nat Cell Biol* 10(7):866-873.
18. Black JC, Mosley A, Kitada T, Washburn M, & Carey M (2008) The SIRT2 deacetylase regulates autoacetylation of p300. *Mol Cell* 32(3):449-455.
19. Arif M, *et al.* (2010) Nitric oxide-mediated histone hyperacetylation in oral cancer: target for a water-soluble HAT inhibitor, CTK7A. *Chem Biol* 17(8):903-913.
20. Teufel DP, Freund SM, Bycroft M, & Fersht AR (2007) Four domains of p300 each bind tightly to a sequence spanning both transactivation subdomains of p53. *Proc Natl Acad Sci U S A* 104(17):7009-7014.

21. Gu W & Roeder RG (1997) Activation of p53 sequence-specific DNA binding by acetylation of the p53 C-terminal domain. *Cell* 90(4):595-606.
22. Liu L, *et al.* (1999) p53 sites acetylated in vitro by PCAF and p300 are acetylated in vivo in response to DNA damage. *Mol Cell Biol* 19(2):1202-1209.
23. Sykes SM, *et al.* (2006) Acetylation of the p53 DNA-binding domain regulates apoptosis induction. *Molecular cell* 24(6):841-851.
24. Tang Y, Luo J, Zhang W, & Gu W (2006) Tip60-dependent acetylation of p53 modulates the decision between cell-cycle arrest and apoptosis. *Molecular cell* 24(6):827-839.
25. Rokudai S, *et al.* (2013) MOZ increases p53 acetylation and premature senescence through its complex formation with PML. *Proc Natl Acad Sci U S A* 110(10):3895-3900.
26. Haaland I, *et al.* (2014) Molecular mechanisms of nutlin-3 involve acetylation of p53, histones and heat shock proteins in acute myeloid leukemia. *Mol Cancer* 13:116.
27. Lambert PF, Kashanchi F, Radonovich MF, Shiekhattar R, & Brady JN (1998) Phosphorylation of p53 serine 15 increases interaction with CBP. *J Biol Chem* 273(49):33048-33053.
28. Lee CW, Ferreon JC, Ferreon AC, Arai M, & Wright PE (2010) Graded enhancement of p53 binding to CREB-binding protein (CBP) by multisite phosphorylation. *Proc Natl Acad Sci U S A* 107(45):19290-19295.
29. Lee CW, Arai M, Martinez-Yamout MA, Dyson HJ, & Wright PE (2009) Mapping the interactions of the p53 transactivation domain with the KIX domain of CBP. *Biochemistry* 48(10):2115-2124.
30. Polley S, *et al.* (2008) Differential recognition of phosphorylated transactivation domains of p53 by different p300 domains. *J Mol Biol* 376(1):8-12.
31. Itahana Y, Ke H, & Zhang Y (2009) p53 Oligomerization is essential for its C-terminal lysine acetylation. *J Biol Chem* 284(8):5158-5164.
32. Yi P, *et al.* (2015) Structure of a biologically active estrogen receptor-coactivator complex on DNA. *Mol Cell* 57(6):1047-1058.
33. Shaikh TR, *et al.* (2008) SPIDER image processing for single-particle reconstruction of biological macromolecules from electron micrographs. *Nat Protoc* 3(12):1941-1974.
34. Delvecchio M, Gaucher J, Aguilar-Gurrieri C, Ortega E, & Panne D (2013) Structure of the p300 catalytic core and implications for chromatin targeting and HAT regulation. *Nat Struct Mol Biol* 20(9):1040-1046.
35. Pettersen EF, *et al.* (2004) UCSF Chimera--a visualization system for exploratory research and analysis. *J Comput Chem* 25(13):1605-1612.
36. Melero R, *et al.* (2011) Electron microscopy studies on the quaternary structure of p53 reveal different binding modes for p53 tetramers in complex with DNA. *Proc Natl Acad Sci U S A* 108(2):557-562.
37. Jiang L, *et al.* (2015) Ferroptosis as a p53-mediated activity during tumour suppression. *Nature* 520(7545):57-62.
38. An W, Kim J, & Roeder RG (2004) Ordered cooperative functions of PRMT1, p300, and CARM1 in transcriptional activation by p53. *Cell* 117(6):735-748.
39. Ceschin DG, *et al.* (2011) Methylation specifies distinct estrogen-induced binding site repertoires of CBP to chromatin. *Genes Dev* 25(11):1132-1146.
40. Wang X & Li S (2016) [Corrigendum] Chromatin immunoprecipitation-sequencing predicts p300 binding sites in the MCF7 human breast cancer cell line. *Int J Mol Med* 38(2):675.

41. Bose DA, *et al.* (2017) RNA Binding to CBP Stimulates Histone Acetylation and Transcription. *Cell* 168(1-2):135-149.e122.
42. Holmqvist PH & Mannervik M (2013) Genomic occupancy of the transcriptional co-activators p300 and CBP. *Transcription* 4(1):18-23.
43. Bach M, *et al.* (2007) Fast set-up of doxycycline-inducible protein expression in human cell lines with a single plasmid based on Epstein-Barr virus replication and the simple tetracycline repressor. *FEBS J* 274(3):783-790.
44. Tang G, *et al.* (2007) EMAN2: An extensible image processing suite for electron microscopy. *J Struct Biol* 157(1):38-46.
45. Sorzano COS, *et al.* (2004) XMIPP: a new generation of an open-source image processing package for electron microscopy. *J Struct Biol* 148(2):194-204.
46. Scheres SHW (2012) RELION: Implementation of a Bayesian approach to cryo-EM structure determination. *J Struct Biol* 180(3):519-530.
47. Patel RK & Jain M (2012) NGS QC Toolkit: a toolkit for quality control of next generation sequencing data. *PLoS One* 7(2):e30619.
48. Langmead B, Trapnell C, Pop M, & Salzberg SL (2009) Ultrafast and memory-efficient alignment of short DNA sequences to the human genome. *Genome Biol* 10(3):R25.
49. Li H, *et al.* (2009) The Sequence Alignment/Map format and SAMtools. *Bioinformatics* 25(16):2078-2079.
50. Feng J, Liu T, Qin B, Zhang Y, & Liu XS (2012) Identifying ChIP-seq enrichment using MACS. *Nat Protoc* 7(9):1728-1740.
51. Robinson JT, *et al.* (2011) Integrative genomics viewer. *Nat Biotechnol* 29(1):24-26.
52. Heinz S, *et al.* (2010) Simple combinations of lineage-determining transcription factors prime cis-regulatory elements required for macrophage and B cell identities. *Mol Cell* 38(4):576-589.
53. Salmon-Divon M, Dvinge H, Tammoja K, & Bertone P (2010) PeakAnalyzer: genome-wide annotation of chromatin binding and modification loci. *BMC Bioinformatics* 11:415.
54. Shen L, Shao N, Liu X, & Nestler E (2014) ngs.plot: Quick mining and visualization of next-generation sequencing data by integrating genomic databases. *BMC Genomics* 15:284.
55. Suzuki A, *et al.* (2014) Aberrant transcriptional regulations in cancers: genome, transcriptome and epigenome analysis of lung adenocarcinoma cell lines. *Nucleic Acids Res* 42(22):13557-13572.

Fig. 1

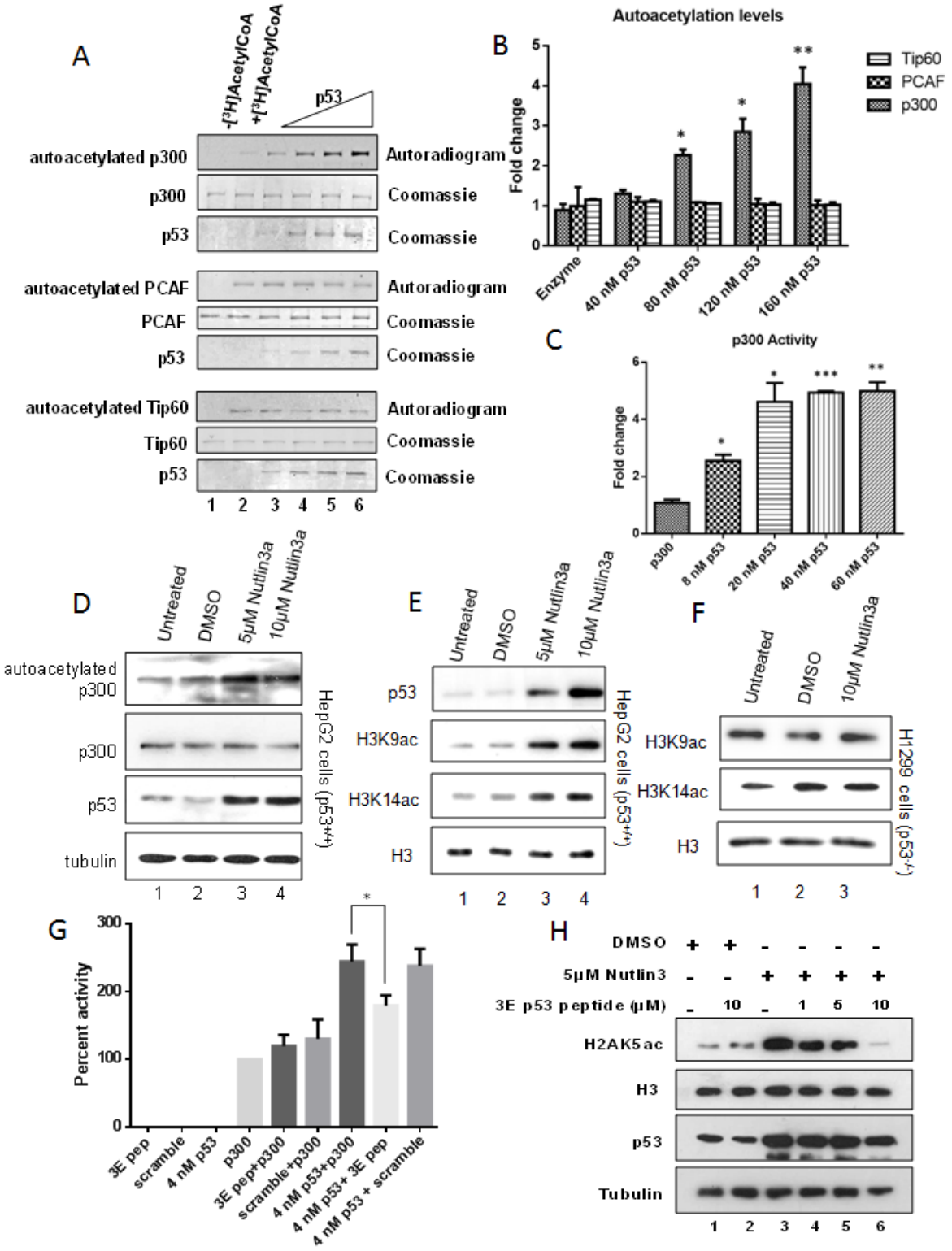
A
-[³H]AcetylCoA
+[³H]AcetylCoA
p53
autoacetylated p300
p300
p53
autoacetylated PCAF
PCAF
p53
autoacetylated Tip60
Tip60
p53
Autoradiogram
Coomassie
1 2 3 4 5 6
B
Autoacetylation levels
Fold change
Tip60
PCAF
p300
Enzyme
40 nM p53
80 nM p53
120 nM p53
160 nM p53
C
p300 Activity
Fold change
p300
8 nM p53
20 nM p53
40 nM p53
60 nM p53
D
Untreated
DMSO
5μM Nutlin3a
10μM Nutlin3a
autoacetylated p300
p300
p53
tubulin
HepG2 cells (p53+/+)
1 2 3 4
E
Untreated
DMSO
5μM Nutlin3a
10μM Nutlin3a
p53
H3K9ac
H3K14ac
H3
HepG2 cells (p53+/+)
1 2 3 4
F
Untreated
DMSO
10μM Nutlin3a
H3K9ac
H3K14ac
H3
H1299 cells (p53-/-)
1 2 3
G
Percent activity
3E pep
scramble
4 nM p53
p300
3E pep+p300
scramble+p300
4 nM p53+p300
4 nM p53+ 3E pep
4 nM p53 + scramble
H
DMSO
5μM Nutlin3
3E p53 peptide (μM)
H2AK5ac
H3
p53
Tubulin
1 2 3 4 5 6

Fig. 2

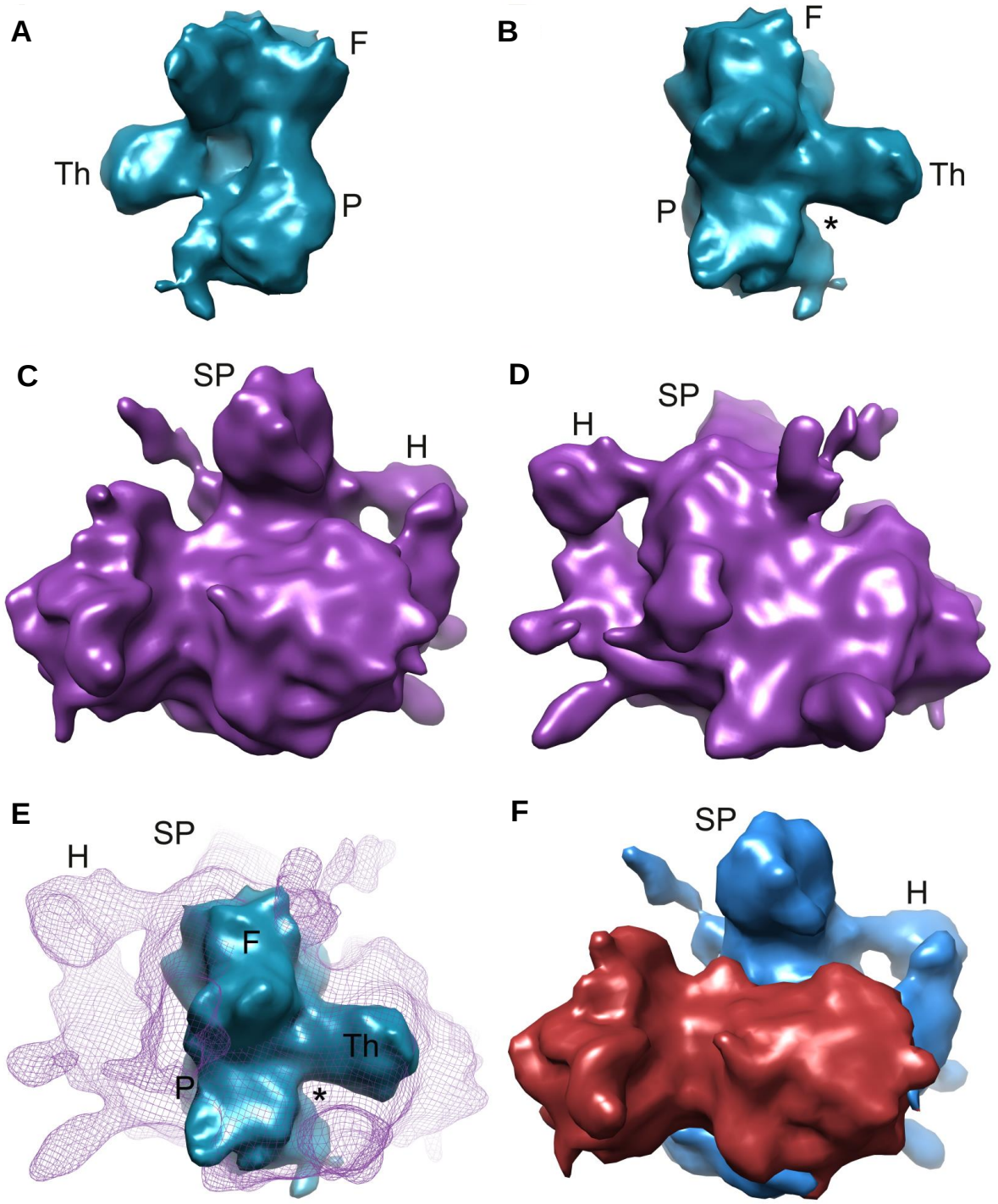

Fig. 3

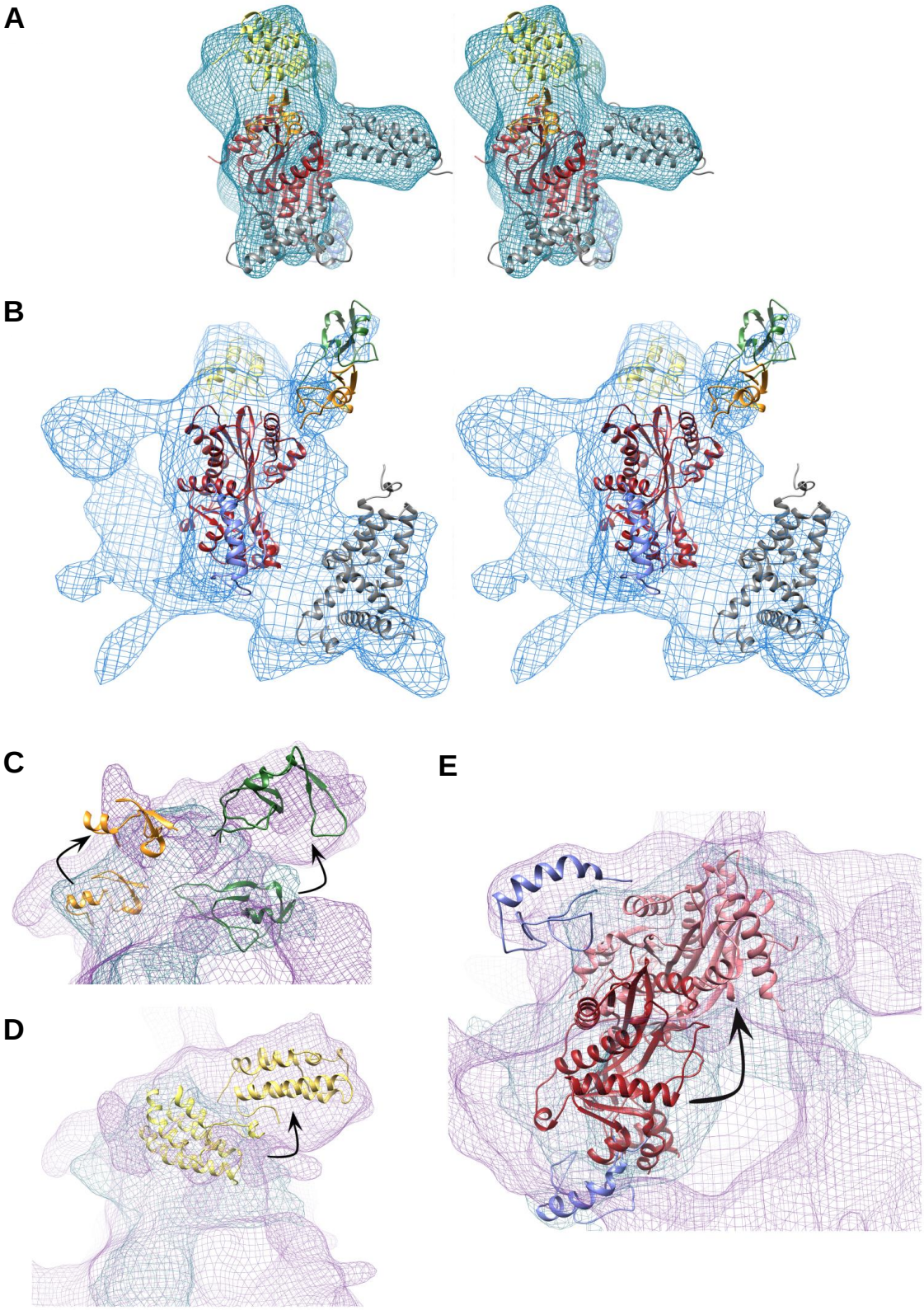

Fig. 4

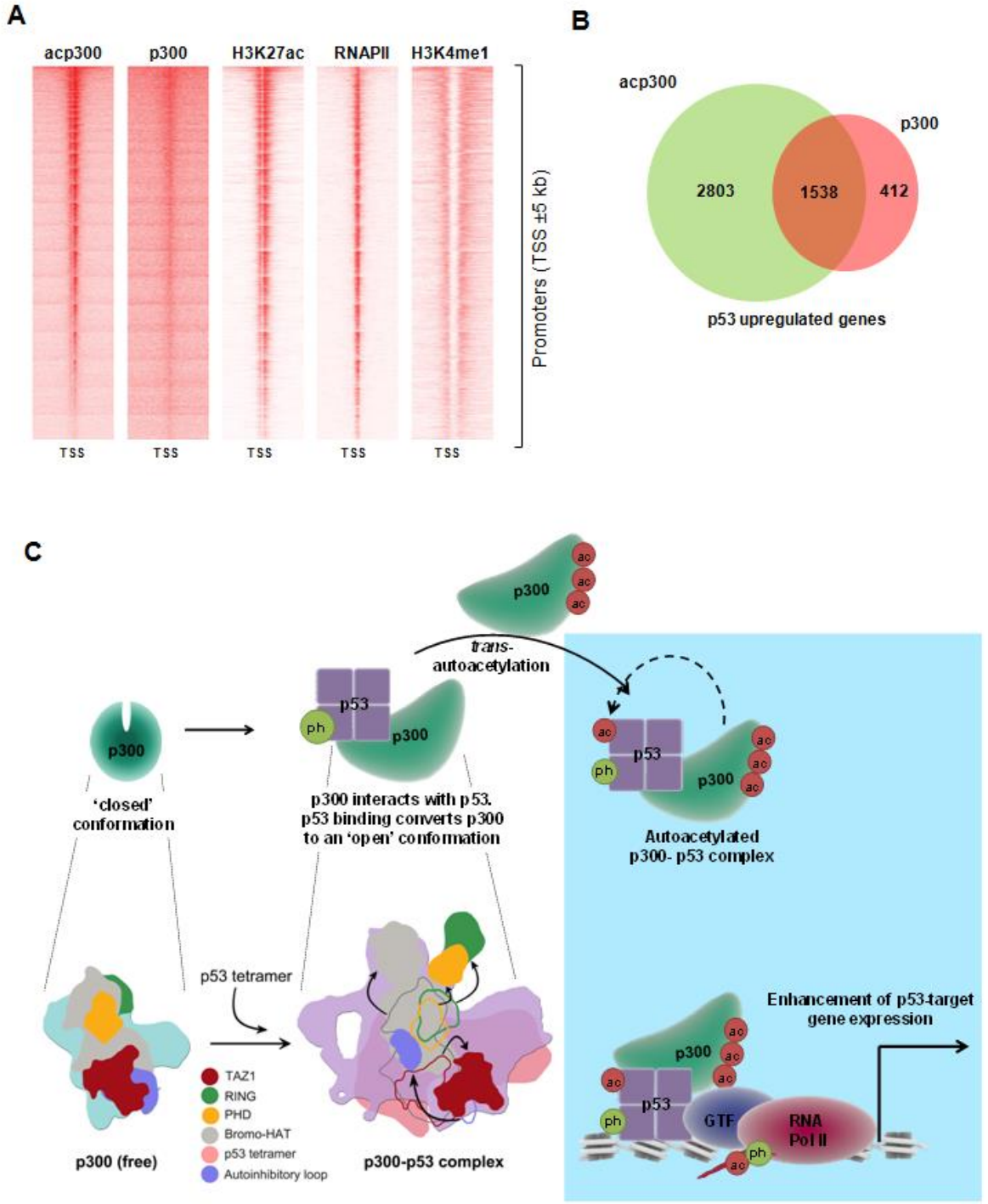
A
acp300
p300
H3K27ac
RNAPII
H3K4me1
TSS
Promoters (TSS ±5 kb)
B
acp300
p300
2803
1538
412
p53 upregulated genes
C
p300
'closed' conformation
p53
ph
p300 interacts with p53. p53 binding converts p300 to an 'open' conformation
trans-autoacetylation
ac
Autoacetylated p300- p53 complex
p53 tetramer
TAZ1
RING
PHD
Bromo-HAT
p53 tetramer
Autoinhibitory loop
p300 (free)
p300-p53 complex
Enhancement of p53-target gene expression
GTF
RNA Pol II